Photoacoustics 23 (2021) 100284

Contents lists available at ScienceDirect

Photoacoustics

journal homepage: www.elsevier.com/locate/pacs

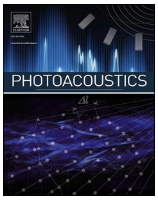

Photostability enhancement of silica-coated gold nanostars for photoacoustic imaging guided photothermal therapy

Yingna Chen [a,1], Chang Xu [b,1], Yu Cheng [b,*], Qian Cheng [a,c,**]

[a] Institute of Acoustics, School of Physics Science and Engineering, Tongji University, Shanghai, PR China
[b] The Institute for Translational Nanomedicine, Shanghai East Hospital, The Institute for Biomedical Engineering & Nano Science, Tongji University School of Medicine, Shanghai, PR China
[c] The Key Laboratory of Spine and Spinal Cord Injury Repair and Regeneration, Ministry of Education, Department of Orthopaedics, Tongji Hospital, Tongji University School of Medicine, Shanghai, PR China

ARTICLE INFO

Keywords:
Gold nanostars
Contrast agent
Photoacoustic imaging
Photostability
Photoacoustic quantitative evaluation

ABSTRACT

Gold nanostars (GNSs) are promising contrast agents for simultaneous photothermal therapy and photoacoustic imaging (PAI) owing to their excellent photothermal conversion efficiency. However, GNSs are easily reshaped under transient high-intensity laser pulses, which can cause a rapid shift in the light absorption peak, resulting in a decrease in both therapeutic and monitoring effects. In this work, we synthesized GNSs without toxic surfactants and coated them with a silica shell to retain their shape, thus maintaining their photostability. The excellent performance of these silica-coated GNSs was verified through both *in vitro* and *in vivo* PAI experiments. The silica-coated GNSs exhibited a threefold improvement in photoacoustic stability, as compared with the non-coated GNSs. The proposed silica coating method for GNSs was found to improve the photostability of GNSs, making them efficient, safe, and reliable nanoparticles for PAI.

1. Introduction

Owing to its monitoring functionalities, photoacoustic imaging (PAI) has gained popularity in different tumor treatment fields, especially for photothermal therapy (PTT) [1–5]. PTT media have excellent photothermal conversion efficiency, making them natural contrast agents for PAI. Among these, gold nanoparticles (GNPs) are highly suitable PAI contrast agents owing to their high light absorption and thermal conversion efficiency [6–10]. Furthermore, due to the surface plasmon resonance effect, GNPs have an optical absorption peak up to five orders of magnitude greater than that of dyes (on a per-particle basis) [11]. Moreover, GNPs exhibit diverse morphologies for various applications, including simple spherical gold nanoparticles [12,13], gold nanorods (GNRs) with adjustable aspect ratios [14], and gold nanocages [15,16]. Among the various types of gold nanostructures, gold nanostars (GNSs) possess many unique features owing to their branched structure [17]. The increased specific surface area and more effective electric field penetration of GNSs lead to a radically enhanced heat production, which can significantly benefit both PTT and PAI [18–20]. However, the high photothermal conversion efficiency of GNPs causes stability problems, particularly for GNSs. Under strong light illumination, the increase in temperature can melt the GNSs, transforming them into nanospheres [14,21–23]. As the spectroscopic optical absorption of GNSs is highly dependent on their morphology, this reshaping under light illumination strongly affects their photothermal (PT) and photoacoustic (PA) stabilities. Consequently, such light illumination-induced changes in morphology limit the use of GNSs as PAI agents.

Since 1996, when Mulvaney et al. performed groundbreaking studies on the compact silica encapsulation of GNPs [24], there has been considerable interest in increasing the stability of GNPs by coating their surface with shells. Different methods of forming silica shells have been proposed [23–26], and different shell materials have been investigated and developed [27,28]. Silica coating affords three main advantages. First, synthesis methods for silica coating are mature and reproducible

---

Abbreviations: GNPs, gold nanoparticles; GNSs, gold nanostars; MSCs, mesenchymal stromal cells; OPO, optical parametric oscillator; PA, photoacoustic; PAI, photoacoustic imaging; PT, photothermal; PTT, photothermal therapeutic.

* Corresponding author.

** Corresponding author at: Institute of Acoustics, School of Physics Science and Engineering, Tongji University, Shanghai, PR China.

E-mail addresses: yucheng@tongji.edu.cn (Y. Cheng), q.cheng@tongji.edu.cn (Q. Cheng).

[1] These authors contributed equally to this study.

https://doi.org/10.1016/j.pacs.2021.100284
Received 13 October 2020; Received in revised form 25 May 2021; Accepted 13 July 2021

even at the mass production level. Second, an ideal and permanent attachment between biomarkers and GNPs can be achieved through the covalent coupling of biomolecules to the surface-functionalized silica coating [29]. Third, the silica coating reduces the thermal resistance between the GNPs and the biological environment, resulting in a stronger PA signal [30,31]. In 2010, Chen et al. [27] studied the PA stability of silica-coated nanomaterials for the first time and demonstrated that sealing nanomaterials in silica shells improves their PA stability under pulsed laser illumination.

To improve the long-term role of GNSs in PAI, it is necessary to improve the PA stability of GNSs. However, the effect of silica shells on the PA stability of GNSs has not been reported thus far. In this study, the PA stability of GNSs coated with silica shells was studied for application in PAI. The improved PA stability of the silica-coated GNSs was characterized, and the thickness of the silica coating was optimized. The PA stability of the GNSs was monitored *in vitro* under continuous irradiation by 600 laser pulses with a light fluence of 23 mJ/cm^2 at a wavelength of 850 nm. The improved PA stability of the silica-coated GNSs was confirmed *in vivo* using a mouse tumor model.

2. Material and methods

2.1. Synthesis of GNSs and silica-coated GNSs

GNSs were synthesized via seed-mediated growth. The seed was obtained by vigorous mixing of 44.6 mg sodium citrate in 1 mM $HAuCl_4$ solution at 100 °C. After a reaction time of 15 min, the solution was wine red. The solution was then cooled to 25 °C. The seed solution was purified via filtration using a 0.22 μm nitrocellulose membrane. The filtered solution was stored at 4 °C for long-term storage. For GNS synthesis, 600 μL of the seed solution was added to 60 mL of 0.25 mM $HAuCl_4$ solution with 0.01 M HCl in a 100 mL glass vial at room temperature under moderate stirring (700 rpm), and immediately, 600 μL of 3 mM $AgNO_3$ and 300 μL of 100 mM acrylic acid were added to the solution. After further stirring for 30 s, the color of the solution rapidly changed from light red to greenish-black, indicating the formation of GNSs. Immediately after the formation of the GNSs, 2 mL HS-PEG-COOH (MW 5000, 5 mg/mL) was added to the solution under gentle stirring for 3 min to ensure adequate diffusion. The mixture was then left standing overnight, resulting in the formation of PEGylated GNSs. The PEGylated GNSs were purified via centrifugation at 9500×*g* for 15 min and then resuspended in double-distilled water.

A modified Stöber method was used to grow a silica shell with a controlled thickness around the GNSs [32,33]. The synthesized PEGylated GNSs were dissolved in 60 % isopropanol solution, and ammonia solution in isopropanol was added slowly to adjust the pH to 11. Thereafter, 100 mM tetraethylorthosilicate (TEOS) in isopropanol solution was slowly injected into the mixture with vigorous stirring. The mixture was stirred for 2 h to complete the coating process. To adjust the thickness of the silica shell, 20–150 μL of TEOS solution was used during the preparation process. The product was purified via centrifugation with double-distilled water and ethanol at 9500 rpm for 15 min.

2.2. Ultraviolet–visible–near-infrared extinction spectroscopy detection and transmission electron microscopy imaging

Ultraviolet–visible–near-infrared (UV–vis–NIR) spectroscopy was used to monitor the absorption peak shift after laser irradiation, enabling a comparison of the light absorbing ability of the silica-coated GNSs and that of non-coated GNSs. The concentration of all GNS samples was 0.2 nM. The morphologies of the silica-coated GNSs and uncoated GNSs after laser irradiation were characterized using transmission electron microscopy (TEM).

2.3. Temperature rise curve

A continuous-wave NIR laser (808 nm, ANJ, Beijing) was chosen for PTT. The laser irradiation was performed with a laser power of 1 W/cm^2 and silica-coated GNSs with different thicknesses (0, 10 nm, 18 nm, 25 nm, and 30 nm) for 15 min. The absorbance value of the silica-coated GNSs at 808 nm was 1. The laser spot was adjusted to cover the entire bottle. While the temperature was increased, thermal images were captured using an infrared thermal camera (DALI, China) at intervals of 1 min. Furthermore, the temperature increase of the silica-coated GNSs was recorded via infrared thermography at intervals of 1 min, for a total of 15 min. Subsequently, the data were sorted and plotted as time––temperature curves. The temperature rise curve of distilled water was considered as the control group.

2.4. Evaluation of silica-coated GNS safety with mesenchymal stromal cell viability measurements

Mesenchymal stromal cells (MSCs) were seeded in 96-well plates and left overnight. Then, the MSCs were incubated with silica-coated GNSs at concentrations of 0, 10, 20, 40, 80, and 160 pM. After 24 h of incubation, the MSC-silica-coated GNSs were rinsed three times with phosphate buffer saline, and the cell viability of the MSCs was measured using the CCK-8 assay.

2.5. In vitro PA experiment

The PA stability of the GNSs as well as the silica-coated GNSs was estimated by quantifying the change in PA signal intensity during laser irradiation. Fig. 1 illustrates the *ex vivo* experimental setup used to measure the PA stability of the materials. At a concentration of 0.2 nM, the GNSs were contained in a highly transparent cylindrical glass tube with an inner diameter of 3 mm, a wall thickness of 1 mm, and a length of 3 cm. The glass tube containing the materials was immersed in water for PA detection. A tunable optical parametric oscillator (OPO) laser (Phocus Mobile, OPOTEK, Carlsbad, CA) was used to generate illumination with a wavelength of 850 nm. The laser beam energy was 18 mJ per pulse and was collimated to approximately 1 cm in diameter (corresponding to a light fluence of 23 mJ/cm^2) with a laser repetition rate of 10 Hz. The duration of laser irradiation was 60 s, which was precisely controlled based on the number of laser pulses. The excited PA signal from the GNSs was received via a hydrophone (HNC-1500, ONDA, Sunnyvale, CA) and amplified by 35 dB using an amplifier (5072PR, OLYMPUS, Waltham, MA). The PA data were then received by an oscilloscope (TDS 3034B, Tektronix, Long Branch, NJ) and finally recorded on a computer through a custom-built LabVIEW program. In the optical path, a 90:10 beam splitter was used to split the laser beam, and the split 10 % light was irradiated on a blackbody. An additional focused transducer (Immersion Transducers, Olympus Corp., Tokyo, Japan) with a center frequency of 5 MHz was used to receive the PA signal generated by the blackbody in order to monitor the laser energy, for the purposes of eliminating the laser energy fluctuations.

2.6. In vivo PA experiment

The *in vivo* PAI experiment was based on a custom-built ultrasound (US) and photoacoustic (PA) dual-modality imaging device (TWPA-I, Tongji University, Shanghai, China & Wisonic, Guangdong, China). The experimental setup is depicted in Fig. 2. The experiment was conducted on tumor-bearing nude mice (five-week old, ~20 g body weight). After injecting 1 million MDA-MB-231 cells in the dorsa of the mice for two weeks, the tumor size reached 5 mm in length; 50 μg of condensed silica-coated GNS solution was injected *in situ* into the center of the tumor. Immediately after injection, the mice were imaged using the US-PA imaging system. During image acquisition, each mouse was anesthetized by injecting 0.8 mL chloral hydrate at a concentration of 10 %

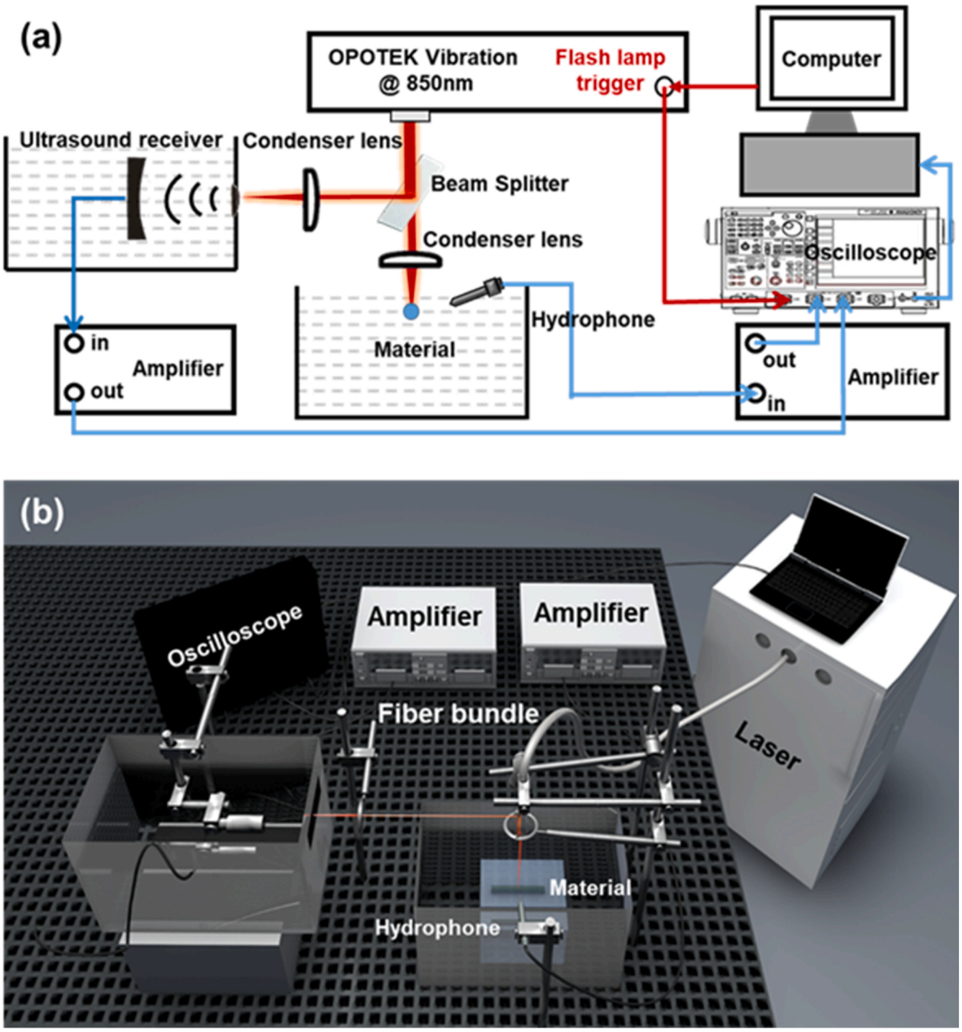

Fig. 1. *In vitro* experiment setup. (a) Schematic diagram of *in vitro* photoacoustic experiment; (b) Schematic diagram of 3D *in vitro* photoacoustic experiment. The laser and the oscilloscope were synchronized.

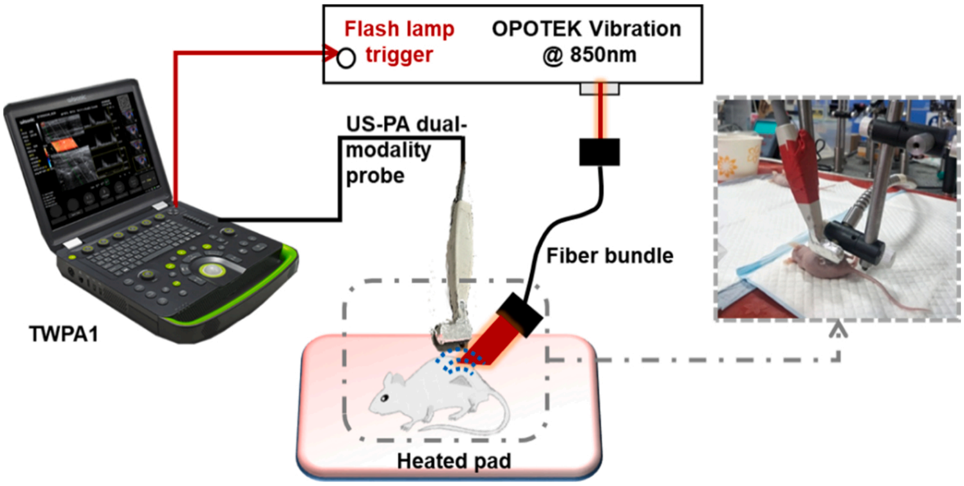

Fig. 2. *In vivo* experiment setup. A home-made US-PA dual-modality device was used to image the tumor with locally injected GNRs.

per species. The anesthetized mice were placed on a heating pad. The imaging linear array probe (LH15-6, Wisonic, Guangdong, China) was fixed above the tumor for PA and US imaging, using ultrasound gel as the coupling material. The OPO laser (Phocus Mobile, OPOTEK, Carlsbad, CA) was used to generate illumination with a wavelength of 850 nm. A laser beam with an energy of 18 mJ per pulse was collimated to approximately 1 cm in diameter (corresponding to a light fluence of 23 mJ/cm^2) and was used to irradiate the mouse tumor from the side through an optical fiber bundle. Considering the light attenuation in biological tissues, the number of laser pulses in the *in vivo* experiment was four times that in the *in vitro* experiment.

2.7. PA signal analysis

All data processing was performed using MATLAB R2019a. For the *in vitro* experiment, the PA signal amplitudes from the material and blackbody were quantified as the peak-to-peak amplitudes. The signal amplitude ratio between the material and the blackbody was used to achieve normalized measurements that eliminated the effect of laser fluctuations. The normalized PA amplitudes from the material during continuous laser irradiation were measured, and the changes in amplitude were calculated. In the *in vivo* experiments, the image area for the quantitative analysis was the region of interest (ROI) determined based on the B-mode images. The sum of the pixel intensities in the ROI during laser irradiation was determined, and the intensity changes were calculated.

3. Results

The synthesis process for GNSs and the silica-coated GNSs is illustrated in Fig. 3a. Typical TEM images of the GNSs without and with silica shells of 25 nm at different magnifications are depicted in Figs. 3b and 3c, respectively. Conformal and uniform silica shells were coated around the GNSs. The added silica layer increased the size of the material from 107 nm to approximately 200 nm (Fig. 3d). The UV–vis–NIR spectra of bare GNSs and silica-coated GNSs are depicted in Fig. 3e. The absorption spectra of bare GNSs and silica-coated GNSs are not significantly different, except that the absorption peak of the silica-coated GNSs has a slight redshift and peaks at 850 nm, which is attributed to the increase in the nanoparticle size.

As the silica shell can hinder electric field penetration and heat transfer and also cause nanoparticle aggregation, thickness control is crucial. Silica-coated GNSs with different silica coating thicknesses were prepared by varying the amount of TEOS solution added during silica growth (20, 50, 90, and 150 μL). Typical TEM images of bare GNSs and silica-coated GNSs with various thicknesses of the silica shells are illustrated in Fig. 4a, and the size distributions are depicted in Fig. 4b. With an increase in the silica layer thickness, the particle dispersion becomes worse. This is reasonable because larger particles are more likely to aggregate. The mean size as well as the standard deviation of the thicknesses of the silica shells are quantified in Fig. 4c. The thicknesses of the silica shells were 9.6 ± 1, 18.3 ± 2.4, 24.5 ± 2.2, and 29.5 ± 3.3, corresponding to TEOS volumes of 20, 50, 90, and 150 μL, respectively. With an increase in the TEOS amount, the particle size increases with the thickness of the silica coating. As expected, the optical absorption peak has a slight redshift because the silica shell layer increases the dielectric constant of the nanoparticles and the surrounding medium [34].

The PA stabilities of GNSs with various thicknesses of silica shells were compared using UV–vis–NIR spectroscopy. The light absorption peaks are good indicators of the change in shape of the GNSs. As depicted in Fig. 5a, after the GNS shape changes, the original light absorption peak of the nanoparticles decreases significantly (red arrow), and a shoulder appears near 500 nm (in the red box), which is consistent

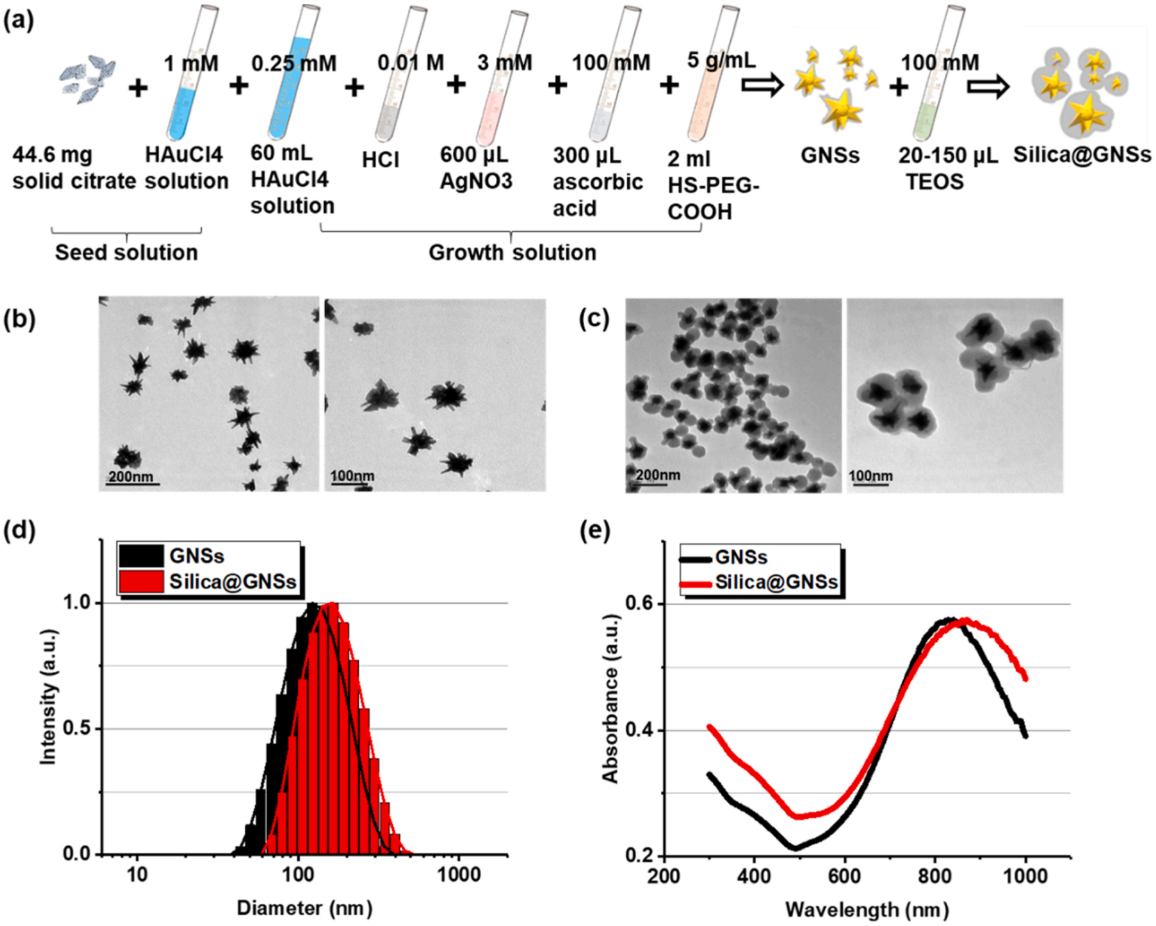

Fig. 3. Synthesis and morphology characterization of GNSs with and without silica shells. (a) Synthesis process of bare GNSs and silica-coated GNSs. (b) TEM images of bare GNSs at different magnifications. (c) TEM images of silica-coated GNSs at different magnifications. (d) Size distribution of bare GNSs and silica-coated GNSs. (e) UV–vis–NIR spectrum of bare GNSs and silica-coated GNSs.

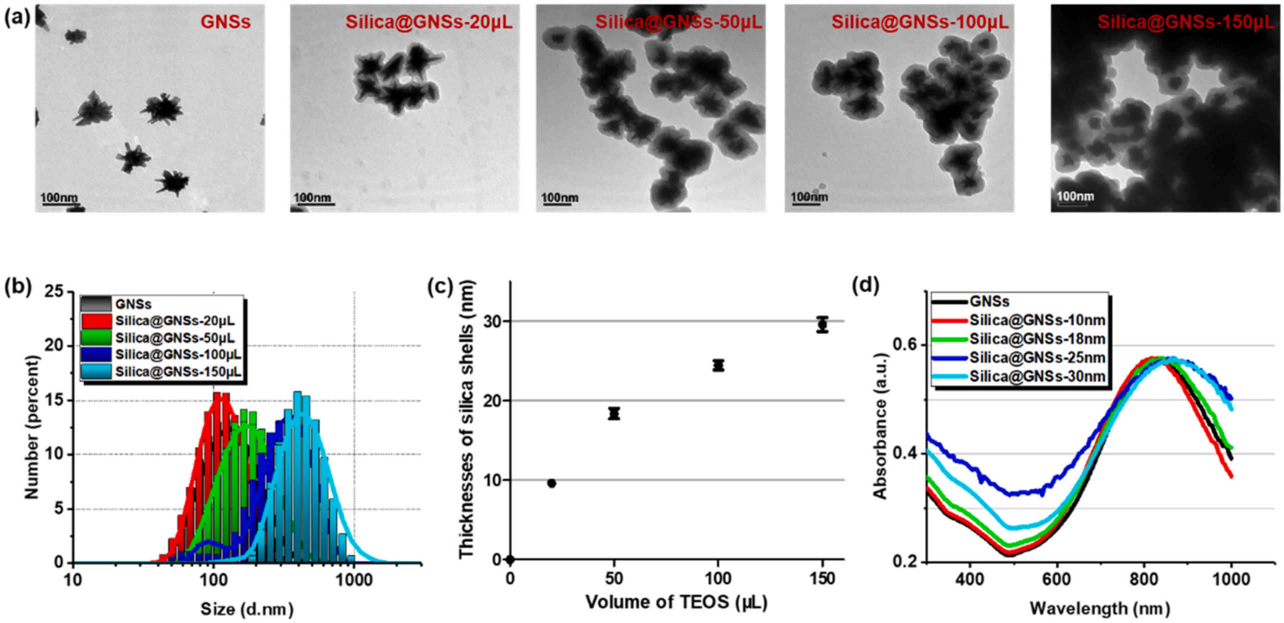

Fig. 4. Morphology and absorption properties of GNSs with various thicknesses of silica shells. (a) TEM images of bare GNSs and silica-coated GNSs with various volumes of TEOS. (b) Statistical size distribution of bare GNSs and silica-coated GNSs with various volumes of TEOS. The pattern of bare GNSs (black) is covered by the pattern of the silica-coated GNSs with 20 μL of TEOS (red) because of their similar size distribution. (c) Thicknesses of silica shells with various volumes of TEOS (mean size ± SD). (d) UV–vis–NIR spectrum of bare GNSs and GNSs with various thicknesses of silica shells (For interpretation of the references to colour in this figure legend, the reader is referred to the web version of this article.).

with the absorption peak of GNSs with the same volume [35]. Each sample, including the bare GNSs and the silica-coated GNSs, exhibits a shape change after sufficient laser pulse irradiation. However, the time duration (i.e., the number of laser pulses) that each sample can tolerate before shape change is initiated differs. Because the pulse repetition rates of different lasers often vary, the number of pulses is preferred for characterizing the stability of materials. Here, the laser pulse repetition frequency was 10 Hz; thus, the number of pulses is 10 times greater than that during laser irradiation. In the experiment, we estimate the deformation of the material by observing the change in color at intervals of 5 s, i.e., 50 pulses. With a thicker silica layer, the GNSs have a higher tolerance to the pulsed laser. As depicted in Fig. 5b, in comparison with the bare GNSs, which underwent a change in shape after 30 s of irradiation (i.e., 300 pulses), the silica-coated GNSs with a 25 nm silica coating maintained their shape up to 180 s of irradiation (i.e., 1800 pulses). Thus, shells thicker than 25 nm can bear more than 1800 laser pulses. Considering the potential for aggregation and the reduction in electric field penetration when using thick silica shells, 25 nm was considered as the optimal silica shell coating thickness. Adding 100 μL TEOS solution during the silica coating process produced GNSs with a 25 ± 2.2 nm-thick silica shell. With regard to PTT, based on analyses of the infrared thermal images (Fig. 5c) and temperature rise curves (Fig. 5d) of the GNSs with different thicknesses of silica coatings, there was no significant difference. This implies that the thickness of the silica coating has little influence on the thermal effect of GNSs in PTT.

The cytotoxicity test results for the thickness-optimized silica-coated GNSs are depicted in Fig. 6a. After 24 h of incubation for the silica-coated GNSs with MSCs, the cell survival rates at all test material concentrations were higher than 80 %, demonstrating the good bio-safety of the silica-coated GNSs. UV–vis–NIR spectroscopy was used to compare the PA stability of the silica-coated GNSs with that of the uncoated GNSs. At the same nanoparticle concentration of 0.2 nM, both samples were irradiated with a pulsed laser for a duration of 60 s at a light fluence of 23 mJ/cm^2 and wavelength of 850 nm. Fig. 6b illustrates the UV–vis–NIR spectra and Fig. 6c depicts the TEM images before and after laser irradiation. The bare GNSs without silica shells were transformed to a spherical shape after the melting of the branches, as is evident from their optical absorption spectra and TEM images. By contrast, protected by the silica coating, the GNSs with 25 nm silica shells exhibited negligible changes in shape and in the optical absorption spectrum after laser irradiation, indicating a significantly improved PA stability.

The PA performances of the GNSs with and without optimized silica shells were compared through *in vivo* and *in vitro* experiments. The stability of the material was quantitatively evaluated by monitoring the change in the PA signal amplitude during laser irradiation. Fig. 7a depicts the variations in the PA amplitude with respect to the pulsed laser irradiation *in vitro* (light fluence of 23 mJ/cm^2 at a wavelength of 850 nm). Moreover, Fig. 7b depicts the quantified attenuation of the PA amplitude after laser irradiation. With laser irradiation, the PA amplitude of the silica-coated GNSs decreases at a significantly lower rate than that of the bare GNSs. The rate of decline in the PA amplitude of the bare GNSs is approximately three times higher than that of the silica-coated GNSs, indicating that the silica-coated GNSs possess better PA stability.

With regard to the *in vivo* experiment, the pixel intensities of the captured images of the mouse tumor model corresponded with the PA signal amplitudes of the locally injected GNSs in the tumors. Figs. 8a and b depict the fused PA and US images from the mouse tumors, one containing bare GNSs and the other containing silica-coated GNSs. Three images in each panel were acquired at 0, 2, and 4 min. In each fusion image, the US image in gray scale in the background shows the tumor structure, and the PA image in pseudo color presents the spatially distributed GNSs in the tumor. As depicted in Fig. 8a, the PA signals from the bare GNSs in the tumor decrease significantly after laser irradiation for 240 s, whereas the PA signals from the silica-coated GNSs in the tumor are considerably more stable during laser irradiation. Figs. 8c and 8d depict the corresponding quantitative results, reflecting the averaged PA signal intensities in the ROIs. These results from the *in vivo* mouse tumor model are consistent with the *in vitro* results, demonstrating that the PA stability of silica-coated GNSs is approximately three times higher than that of the bare GNSs.

4. Discussion

As the silica layer has been proven to improve the photoacoustic

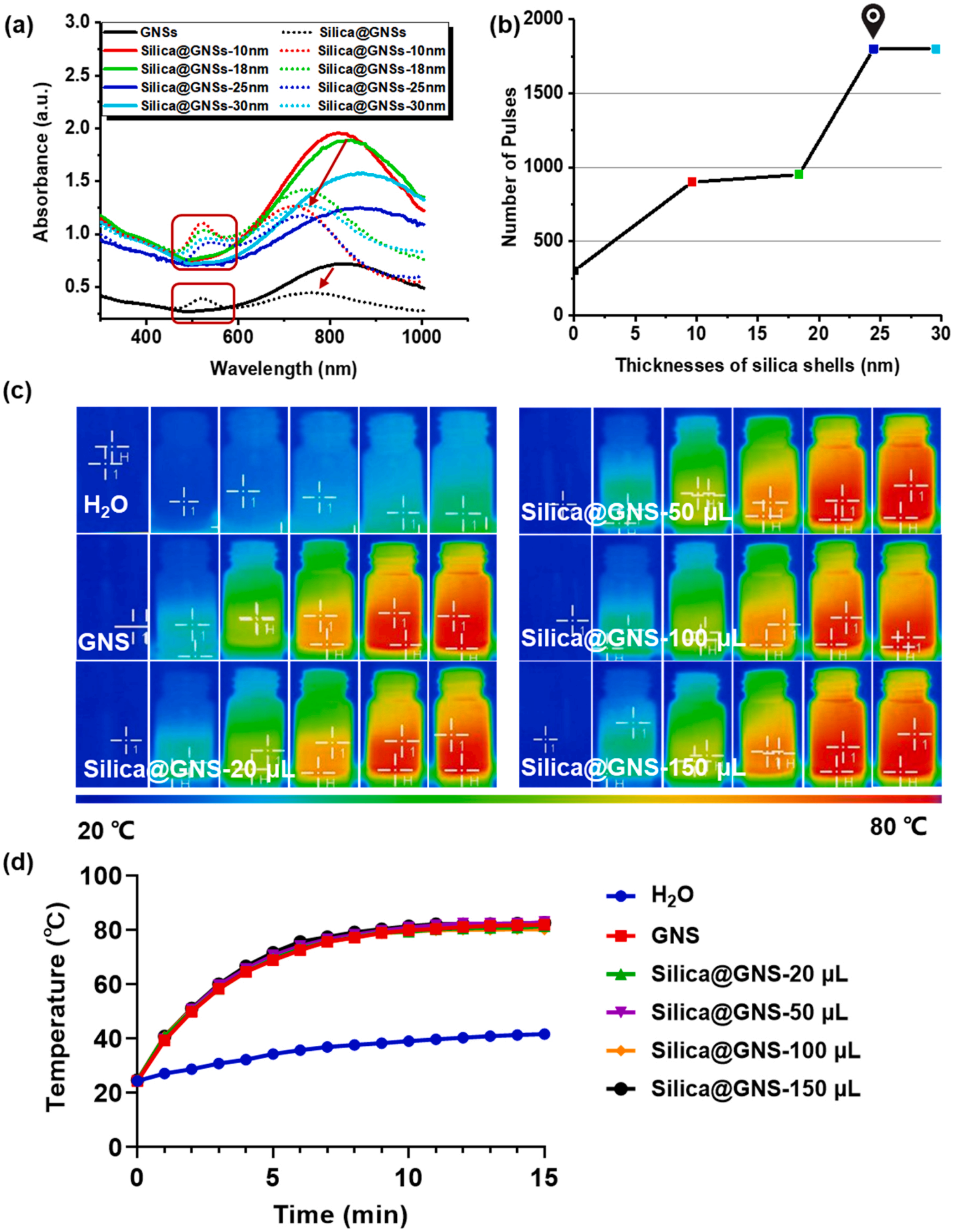

Fig. 5. PA stabilities of GNSs with various thicknesses of silica shells. (a) UV–vis–NIR spectrum of GNSs and silica-coated GNSs with different thicknesses (10 nm, 18 nm, 25 nm, and 30 nm) of silica coating before (solid lines) and after (dot lines) shape change induced by laser irradiation. (b) Number of laser pulse irradiations before shape change occurs for each GNSs sample, including bare GNSs and silica-coated GNSs with different coating thicknesses (i.e., 10 nm, 18 nm, 25 nm, and 30 nm). (c) Infrared thermal images and (d) Temperature increasing curves of GNSs and silica-coated GNSs with different thicknesses (10 nm, 18 nm, 25 nm, and 30 nm) of silica coating.

stability of GNPs, many experiments have adopted silica coatings on differently shaped GNPs to improve their stability, in order to realize longer detection times [20]. Especially for GNSs, which have extremely high light-to-heat conversion efficiencies but are unstable, the silica coating shows its importance and effectiveness. Researchers have also obtained good results based on this method [33]. This result is widely accepted, but there is limited research highlighting the extent to which a silica shell can improve the stability of GNSs. Our research, as presented above, has shown that 25 nm-thick silica layers are suitable for biological experiments and afford a threefold improvement in the stability of GNSs, as compared to bare GNSs.

However, it is necessary to note that, for the sake of safety, a smaller

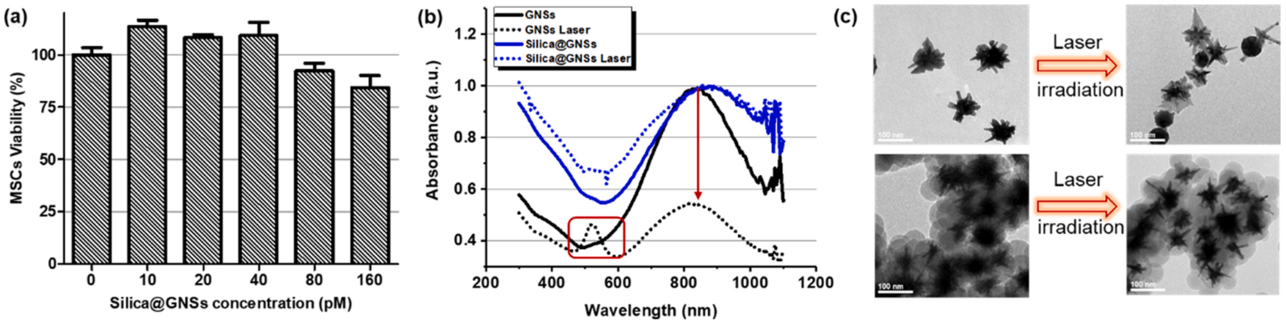

Fig. 6. Cytotoxicity and PA stability of GNSs with silica shells at the optimized thickness (i.e., 25 nm). (a) Cell viability with different concentrations of silica-coated GNSs. (b) Comparison of UV–vis–NIR spectra of bare GNSs and silica-coated GNSs (25 nm coating) before (solid lines) and after (dotted lines) 60-second laser irradiation. (c) TEM images of bare GNSs and silica-coated GNSs before and after laser irradiation.

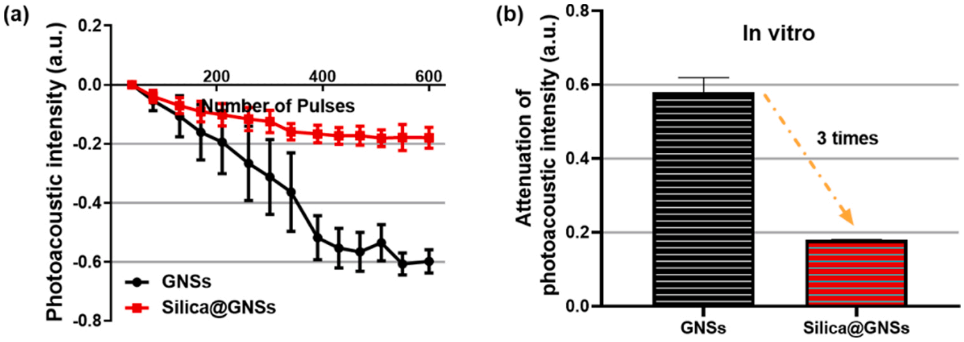

Fig. 7. *In vitro* measurements of PA signal amplitudes of GNSs with and without silica shells during laser irradiation. (a) PA signal amplitudes from bare GNSs (black circles) and silica-coated GNSs (red squares) during laser irradiation. (b) Attenuations of PA signal amplitudes from bare GNSs and silica-coated GNSs after laser irradiation (For interpretation of the references to colour in this figure legend, the reader is referred to the web version of this article).

silica shell thickness was chosen in this study instead of a larger one, which is more likely to aggregate. Previous studies have shown that agglomerated nanoparticles can enhance photoacoustic signals efficiently owing to their superior thermal diffusion and thermal dynamic properties, as compared with discrete particles [37]. However, safety problems also arise, such as it is difficult to inject the agglomerated clusters during application experiments for accumulation in the lung or kidney areas. In addition, studies have shown that excessively thick silicon dioxide layers directly reduce the photoacoustic signal intensities of discrete nanoparticles owing to the reduced local energy fluence and increased scattering [38]. It remains unclear whether the reduction in a single particle signal can be compensated by the energy increase after aggregation. Considering these factors, a silicon dioxide shell with smaller thickness adopted in this study.

Finally, to popularize the use of this approach in clinical settings, further research and efforts need to be devoted toward the clinical conversion of nanomaterials. As is evident, safety issues are the primary obstacles to clinical conversion. Moreover, given that no unified standard for the use and safety of nanomaterials is currently available, it is difficult to evaluate the safety of different nanomaterials; this, in turn, hinders their clinical conversion [39]. Nevertheless, gold nanomaterials, which can be nondestructively tested using PAI, can be traced in the body and can be better evaluated for safety, as compared to materials that are difficult to trace and cannot be evaluated. Furthermore, in terms of the performance of the silica-coated nanostars, the possibility of clinical transformation is expected to be considerably high, once the *in vivo* safety has been confirmed. The excellent photothermal conversion efficiency of silica-coated nanostars makes them highly suitable for use as PTT media; moreover, they are non-toxic, comprise a biocompatible metal core, can be easily synthesized, and possess multiple surface functionalities [40]. This enhanced stability allows for longer monitoring and better control over safety. Lastly, it is important to note that, although the clinical transformation of nanomaterials is difficult, there have been previous successes, including metallic nanotechnology (NBTXR3/Hensify) [41]. Therefore, the clinical conversion of silica-coated nanostars is considered feasible, albeit at the cost of long-term promotion.

5. Conclusion

In this study, silica shells were employed to coat GNSs in order to enhance their PA stabilities. As the thickness of the silica shell affects aggregation and electric field penetration, the silica shell thickness must be optimized. A 25 nm-thick silica layer is considered to provide the best tradeoff among stability, safety, and dispersion. Based on *in vitro* and *in vivo* PA experiments, we demonstrated that the 25 nm-thick silica shell significantly improves the structural stability of GNSs. The high structural stability and excellent PA performance of the silica-coated GNSs are suitable for longer-term PAI monitoring. Moreover, the surface of the silica shells can be easily functionalized to promote the accumulation of GNSs in tumors, thereby increasing the efficiency of PTT and improving the performance of PAI. In addition to this study, several other studies have also investigated the combination of GNSs with stem cells for diagnosing and treating tumors [42,43]. These studies reveal that stem cells can promote the accumulation and dispersion of GNSs in tumors through the tumor-homing effect.

Although the importance of the silica shell in improving PA stability has been demonstrated, many challenges still need to be overcome to improve the practicality of silica-coated GNSs for imaging diagnostics and nanoparticle-mediated therapies. In the future, we intend to establish a physical model of silica-coated GNSs, which can help further optimize the silica coating thickness and strengthen the PA and photothermal effects. Furthermore, the effect of the size of the silica-coated GNSs on cellular uptake and metabolism should also be considered for

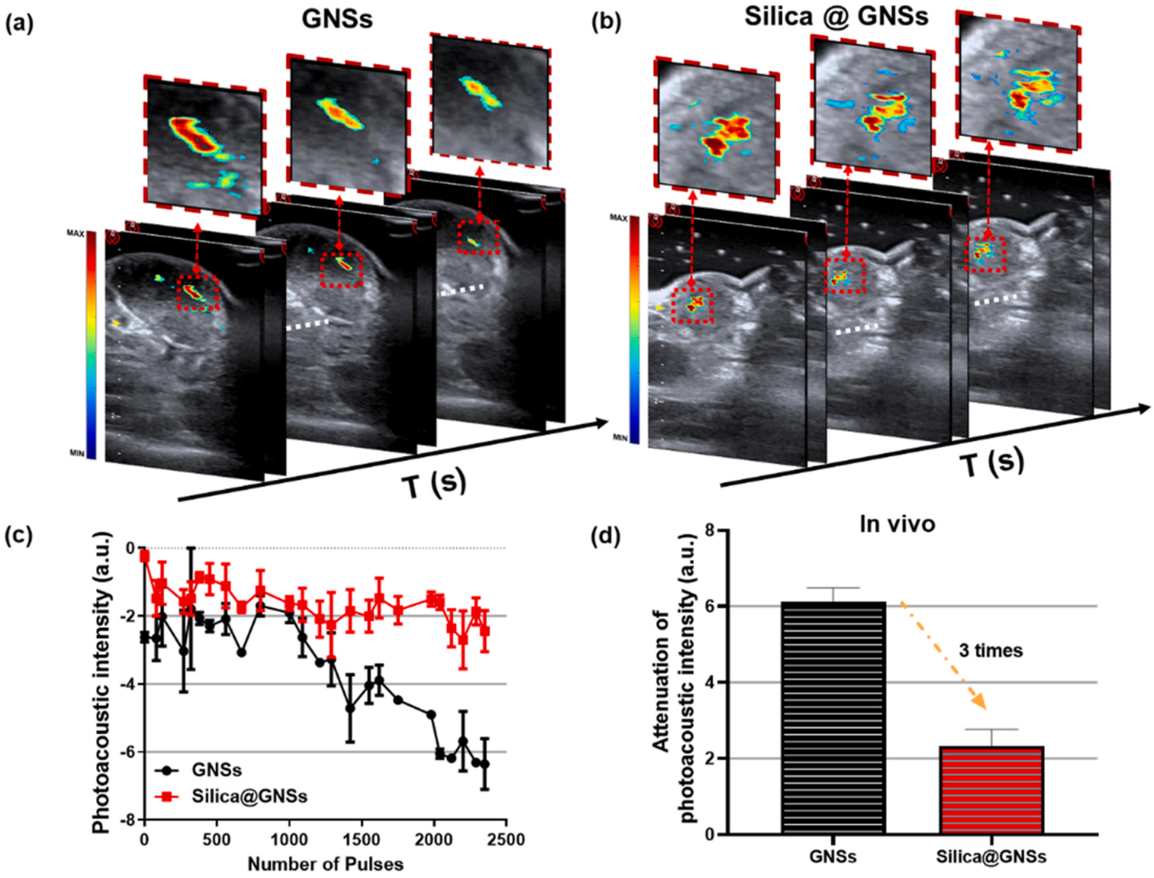

Fig. 8. *In vivo* PA test results of the stabilities of GNSs with and without silica shells. (a) US and PA fused images of a mouse tumor containing bare GNSs, showing the decreasing of the PA signal intensities from the GNSs during laser irradiation. (b) US and PA fused images of a mouse tumor containing silica-coated GNSs, demonstrating improved stability during laser irradiation. (c) Average PA pixel intensities in the ROI in the tumors as a function of time during laser irradiation. The measurement from bare GNSs (black circles) is compared to that from the silica-coated GNSs (red squares). (d) Attenuation of PA signal intensities from bare GNSs and silica-coated GNSs measured in tumors *in vivo* during laser irradiation (For interpretation of the references to colour in this figure legend, the reader is referred to the web version of this article).

potential applications *in vivo*, such as when silica-coated GNSs are used with stem cells. We also hope to promote the implementation of unified testing standards for nanoparticles, in order to realize the clinical transformation of materials under these standards.

Funding

This work was supported by the National Natural Science Foundation of China [grant numbers 12034015 and 11674249] and the National Key Research and Development Program of China [grant number 2017YFC0111400 and 2016YFA0100800].

CRediT authorship contribution statement

Yingna Chen: Methodology, Formal analysis, Validation, Writing - original draft. **Chang Xu:** Resources, Data curation, Formal analysis. **Yu Cheng:** Project administration, Supervision. **Qian Cheng:** Conceptualization, Writing - review & editing, Funding acquisition.

Declaration of Competing Interest

The authors report no declarations of interest.

Acknowledgment

We would like to thank Editage (www.editage.cn) for English language editing.

References

[1] C. Dong, Q. Jiang, X. Qian, W. Wu, W. Wang, L. Yu, Y. Chen, A self-assembled carrier-free nanosonosensitizer for photoacoustic imaging-guided synergistic chemo–sonodynamic cancer therapy, Nanoscale 12 (2020) 5587–5600, https://doi.org/10.1039/C9NR10735E.

[2] Y. Liu, P. Bhattarai, Z. Dai, X. Chen, Photothermal therapy and photoacoustic imaging *via* nanotheranostics in fighting cancer, Chem. Soc. Rev. 48 (2019) 2053–2108, https://doi.org/10.1039/C8CS00618K.

[3] S. Mallidi, G.P. Luke, S. Emelianov, Photoacoustic imaging in cancer detection, diagnosis, and treatment guidance, Trends Biotechnol. 29 (2011) 213–221, https://doi.org/10.1016/j.tibtech.2011.01.006.

[4] C. Moore, J.V. Jokerst, Strategies for image-guided therapy, surgery, and drug delivery using photoacoustic imaging, Theranostics 9 (2019) 1550–1571, https://doi.org/10.7150/thno.32362.

[5] X. Men, F. Wang, H. Chen, Y. Liu, X. Men, Y. Yuan, Z. Zhang, D. Gao, C. Wu, Z. Yuan, Ultrasmall semiconducting polymer dots with rapid clearance for second near-infrared photoacoustic imaging and photothermal cancer therapy, Adv. Funct. Mater. 30 (2020), https://doi.org/10.1002/adfm.201909673, 1909673.

[6] L. Tong, Q. Wei, A. Wei, J.-X. Cheng, Gold nanorods as contrast agents for biological imaging: optical properties, surface conjugation and photothermal effects, Photochem. Photobiol. 85 (2009) 21–32, https://doi.org/10.1111/j.1751-1097.2008.00507.x.

[7] X. Cheng, R. Sun, L. Yin, Z. Chai, H. Shi, M. Gao, Light-triggered assembly of gold nanoparticles for photothermal therapy and photoacoustic imaging of tumors in vivo, Adv. Mater. 29 (2017), https://doi.org/10.1002/adma.201604894, 1604894.

[8] P. Huang, J. Lin, W. Li, P. Rong, Z. Wang, S. Wang, X. Wang, X. Sun, M. Aronova, G. Niu, R.D. Leapman, Z. Nie, X. Chen, Biodegradable gold nanovesicles with an ultrastrong plasmonic coupling effect for photoacoustic imaging and photothermal therapy, Angew. Chemie 125 (2013) 14208–14214, https://doi.org/10.1002/ange.201308986.

[9] L. Jing, X. Liang, Z. Deng, S. Feng, X. Li, M. Huang, C. Li, Z. Dai, Prussian blue coated gold nanoparticles for simultaneous photoacoustic/CT bimodal imaging and photothermal ablation of cancer, Biomaterials 35 (2014) 5814–5821, https://doi.org/10.1016/j.biomaterials.2014.04.005.

[10] H.-W. Yang, H.-L. Liu, M.-L. Li, I.-W. Hsi, C.-T. Fan, C.-Y. Huang, Y.-J. Lu, M.-Y. Hua, H.-Y. Chou, J.-W. Liaw, C.-C.M. Ma, K.-C. Wei, Magnetic gold-nanorod/PNIPAAmMA nanoparticles for dual magnetic resonance and photoacoustic imaging and targeted photothermal therapy, Biomaterials 34 (2013) 5651–5660, https://doi.org/10.1016/j.biomaterials.2013.03.085.

[11] H.-C. Huang, S. Barua, G. Sharma, S.K. Dey, K. Rege, Inorganic nanoparticles for cancer imaging and therapy, J. Control. Release 155 (2011) 344–357, https://doi.org/10.1016/j.jconrel.2011.06.004.

[12] J. Turkevich, P.C. Stevenson, J. Hillier, A study of the nucleation and growth processes in the synthesis of colloidal gold, Discuss. Faraday Soc. 11 (1951) 55, https://doi.org/10.1039/df9511100055.

[13] M. Brust, M. Walker, D. Bethell, D.J. Schiffrin, R. Whyman, Synthesis of thiol-derivatised gold nanoparticles in a two-phase Liquid–Liquid system, J. Chem. Soc. Chem. Commun. 0 (1994) 801–802, https://doi.org/10.1039/C39940000801.

[14] S.-S. Chang, C.-W. Shih, C.-D. Chen, W.-C. Lai, C.R.C. Wang, The shape transition of gold nanorods, Langmuir 15 (1999) 701–709, https://doi.org/10.1021/la980929l.

[15] J. Chen, J.M. McLellan, A. Siekkinen, Y. Xiong, Z.-Y. Li, Y. Xia, Facile synthesis of gold−Silver nanocages with controllable pores on the surface, J. Am. Chem. Soc. 128 (2006) 14776–14777, https://doi.org/10.1021/ja066023g.

[16] J. Chen, F. Saeki, B.J. Wiley, H. Cang, M.J. Cobb, Z.-Y. Li, L. Au, H. Zhang, M. B. Kimmey, Y.Xia Li, Gold nanocages: bioconjugation and their potential use as optical imaging contrast agents, Nano Lett. 5 (2005) 473–477, https://doi.org/10.1021/nl047950t.

[17] B. Van de Broek, N. Devoogdt, A. D'Hollander, H.-L. Gijs, K. Jans, L. Lagae, S. Muyldermans, G. Maes, G. Borghs, Specific cell targeting with nanobody conjugated branched gold nanoparticles for photothermal therapy, ACS Nano 5 (2011) 4319–4328, https://doi.org/10.1021/nn1023363.

[18] C.L. Nehl, H. Liao, J.H. Hafner, Optical properties of star-shaped gold nanoparticles, Nano Lett. 6 (2006) 683–688, https://doi.org/10.1021/nl052409y.

[19] G. Baffou, R. Quidant, C. Girard, Heat generation in plasmonic nanostructures: influence of morphology, Appl. Phys. Lett. 94 (2009) 153109, https://doi.org/10.1063/1.3116645.

[20] F. Hao, C.L. Nehl, J.H. Hafner, P. Nordlander, Plasmon resonances of a gold nanostar, Nano Lett. 7 (2007) 729–732, https://doi.org/10.1021/nl062969c.

[21] Y.-S. Chen, W. Frey, S. Kim, K. Homan, P. Kruizinga, K. Sokolov, S. Emelianov, Enhanced thermal stability of silica-coated gold nanorods for photoacoustic imaging and image-guided therapy, Opt. Express 18 (2010) 8867, https://doi.org/10.1364/OE.18.008867.

[22] M.B. Mohamed, K.Z. Ismail, S. Link, M.A. El-Sayed, Thermal reshaping of gold nanorods in Micelles, J. Phys. Chem. B 102 (1998) 9370–9374, https://doi.org/10.1021/jp9831482.

[23] H. Petrova, J. Perez Juste, I. Pastoriza-Santos, G.V. Hartland, L.M. Liz-Marzán, P. Mulvaney, On the temperature stability of gold nanorods: comparison between thermal and ultrafast laser-induced heating, Phys. Chem. Chem. Phys. 8 (2006) 814–821, https://doi.org/10.1039/B514644E.

[24] L.M. Liz-Marzán, M. Giersig, P. Mulvaney, Synthesis of nanosized gold−silica core−shell particles, Langmuir. 12 (1996) 4329–4335, https://doi.org/10.1021/la9601871.

[25] H.-Y. Wu, M. Liu, M.H. Huang, Direct synthesis of branched gold nanocrystals and their transformation into spherical nanoparticles, J. Phys. Chem. B 110 (2006) 19291–19294, https://doi.org/10.1021/jp063711d.

[26] T.K. Sau, A.L. Rogach, M. Döblinger, J. Feldmann, One-step high-yield aqueous synthesis of size-tunable multispiked gold nanoparticles, Small 7 (2011) 2188–2194, https://doi.org/10.1002/smll.201100365.

[27] Y.-S. Chen, W. Frey, S. Kim, K. Homan, P. Kruizinga, K. Sokolov, S. Emelianov, Enhanced thermal stability of silica-coated gold nanorods for photoacoustic imaging and image-guided therapy, Opt. Express 18 (2010) 8867, https://doi.org/10.1364/OE.18.008867.

[28] J. Li, J. Han, T. Xu, C. Guo, X. Bu, H. Zhang, L. Wang, H. Sun, B. Yang, Coating urchinlike gold nanoparticles with polypyrrole thin shells to produce photothermal agents with high stability and photothermal transduction efficiency, Langmuir 29 (2013) 7102–7110, https://doi.org/10.1021/la401366c.

[29] S.H. Liu, M.Y. Han, Synthesis, functionalization, and bioconjugation of monodisperse, silica-coated gold nanoparticles: robust bioprobes, Adv. Funct. Mater. 15 (2005) 961–967, https://doi.org/10.1002/adfm.200400427.

[30] H. Moon, D. Kumar, H. Kim, C. Sim, J.-H. Chang, J.-M. Kim, H. Kim, D.-K. Lim, Amplified photoacoustic performance and enhanced photothermal stability of reduced graphene oxide coated gold nanorods for sensitive photoacoustic imaging, ACS Nano 9 (2015) 2711–2719, https://doi.org/10.1021/nn506516p.

[31] Y.-S. Chen, W. Frey, S. Aglyamov, S. Emelianov, Environment-dependent generation of photoacoustic waves from plasmonic nanoparticles, Small 8 (2012) 47–52, https://doi.org/10.1002/smll.201101140.

[32] W. Stöber, A. Fink, E. Bohn, Controlled growth of monodisperse silica spheres in the micron size range, J. Colloid Interface Sci. 26 (1968) 62–69, https://doi.org/10.1016/0021-9797(68)90272-5.

[33] Y. Lu, Y. Yin, B.T. Mayers, Y. Xia, Modifying the surface properties of superparamagnetic iron oxide nanoparticles through a sol−gel approach, Nano Lett. 2 (2002) 183–186, https://doi.org/10.1021/nl015681q.

[34] S. Atta, T.V. Tsoulos, L. Fabris, Shaping gold nanostar electric fields for surface-enhanced raman spectroscopy enhancement via silica coating and selective etching, J. Phys. Chem. C 120 (2016) 20749–20758, https://doi.org/10.1021/acs.jpcc.6b01949.

[35] F. Frederix, J.-M. Friedt, K.-H. Choi, W. Laureyn, A. Campitelli, D. Mondelaers, G. Maes, G. Borghs, Biosensing based on light absorption of nanoscaled gold and silver particles, Anal. Chem. 75 (2003) 6894–6900, https://doi.org/10.1021/ac0346609.

[37] C.L. Bayer, S.Y. Nam, Y.-S. Chen, S.Y. Emelianov, Photoacoustic signal amplification through plasmonic nanoparticle aggregation, J. Biomed. Opt. 18 (2013), 016001, https://doi.org/10.1117/1.JBO.18.1.016001.

[38] Y.-S. Chen, W. Frey, S. Kim, P. Kruizinga, K. Homan, S. Emelianov, Silica-coated gold nanorods as photoacoustic signal nanoamplifiers, Nano Lett. 11 (2011) 348–354, https://doi.org/10.1021/nl1042006.

[39] R. Foulkes, E. Man, J. Thind, S. Yeung, A. Joy, C. Hoskins, The regulation of nanomaterials and nanomedicines for clinical application: current and future perspectives, Biomater. Sci. 8 (2020) 4653–4664, https://doi.org/10.1039/D0BM00558D.

[40] Y. Lara, T. Nguyen, L. Marilena, M. Alexander, Toxicological considerations of clinically applicable nanoparticles, Nano Today 6 (2011) 585–607.

[41] A.C. Anselmo, S. Mitragotri, Nanoparticles in the clinic: an update, Bioeng. Transl. Med. 4 (2019), https://doi.org/10.1002/btm2.10143.

[42] C. Xu, Q. Feng, H. Yang, G. Wang, L. Huang, Q. Bai, C. Zhang, Y. Wang, Y. Chen, Q. Cheng, M. Chen, Y. Han, Z. Yu, M.S. Lesniak, Y. Cheng, A light-triggered mesenchymal stem cell delivery system for photoacoustic imaging and chemo-photothermal therapy of triple negative breast cancer, Adv. Sci. 5 (2018), https://doi.org/10.1002/advs.201800382, 1800382.

[43] R.L. Shammas, A.M. Fales, B.M. Crawford, A.J. Wisdom, G.R. Devi, D.A. Brown, T. Vo-Dinh, S.T. Hollenbeck, Human adipose-derived stem cells labeled with plasmonic gold nanostars for cellular tracking and photothermal cancer cell ablation, Plast. Reconstr. Surg. 139 (2017) 900e–910e, https://doi.org/10.1097/PRS.0000000000003187.

Yingna Chen is currently a Ph.D. student in the Institute of Acoustics of School of Physics Science and Engineering at Tongji University at Shanghai, China. Her research interests are in the clinical translation of photoacoustic imaging and spectrum analysis.

Chang Xu, M.Sc is a PhD student at school of medical at Tongji University. She received her M.Sc in biomedical engineering from Tongji University, China. Her scientific interests cover gold and magnetic nanoparticles design and biomedical application.

Yu Cheng studied Organic Chemistry at Wuhan University in China and received her Ph.D. from Case Western Reserve University. She served as professor and vice-president of the medical school of Tongji University. Her work focuses on magnetic nanomaterials for brain tumors mechanical therapy, and application of nanomaterials and stem cells in cancer therapy; Design and biomedical application of micro-nano robot based on magnetic nanomaterials.

Qian Cheng received the B.S. degree in physics, M.S. and PhD degree in acoustics from Tongji University, China, in 2000, 2003 and 2006, respectively. She is currently a professor at Tongji University. Since 2006, her research interests were optoacoustic phenomena, near-field acoustic imaging technique, Schlieren imaging technique and the development of the acoustic detecting instruments. Her most recent research has focused on the clinical translation of photoacoustic imaging and quantitative analysis, and in particular for tumor diagnosis and evaluation.